

pubs.acs.org/cm Article

Bio-Inspired Degradable Polyethylenimine/Calcium Phosphate Micro-/Nano-Composites for Transient Ultrasound and Photoluminescence Imaging

Tengyu He, David G. Bradley, Ming Xu, Shu-Ting Ko, Baiyan Qi, Yi Li, Yong Cheng, Zhicheng Jin, Jiajing Zhou, Lekshmi Sasi, Lei Fu, Zhuohong Wu, Jingcheng Zhou, Wonjun Yim, Yu-Ci Chang, John V. Hanna, Jian Luo, and Jesse V. Jokerst*



Cite This: Chem. Mater. 2022, 34, 7220-7231



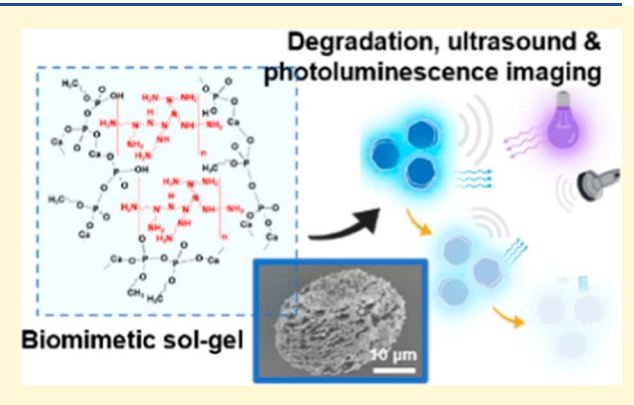
ACCESS

III Metrics & More

Article Recommendations

Supporting Information

ABSTRACT: Inorganic nanomaterials hold immense potential in theranostics, but their translation is limited by the toxicity resulting from non-degradability. Bulk phosphate-based glasses offer great biodegradability, biocompatibility, and ease in incorporating imaging dyes and drugs. However, the facile and mild solution-based synthesis of micro-/nanoparticles of this material is yet to be explored. Inspired by the biosilicification process in the diatom, we created polyethylenimine (PEI)/phosphate aggregates via the hydrogen bonding between amine (PEI) and hydroxyl (phosphate) groups, which was proved by dynamic light scattering and ¹H solution nuclear magnetic resonance. The sol—gel reaction between the calcium precursor and PEI/phosphate aggregates yielded degradable PEI/calcium phosphate (PEI/CP) micro-/nano-composites with versatile



sizes (396 \pm 128 nm to 63 \pm 8 μ m) and morphologies (hexagonal micro-disc, micro-flower, micro-leaf, nano-butterfly, and nano-ribbon). The PEI/CP composition and chemical structure were examined. PEI/CP has negligible cell cytotoxicity and degrades within 24 h. In vitro studies showed the promise for PEI/CP in transient ultrasound and photoluminescence imaging.

INTRODUCTION

Inorganic nanomaterials hold immense potential in theranostics. 1-11 Specific for bioimaging, inorganic nanomaterials have the advantage of controllable size, chemically functionalizable surfaces, and unique physical properties creating imaging signals. For example, gold nanoparticles are a versatile imaging agent for photoacoustic imaging owing to surface plasmon resonance. Semiconducting quantum dots have tunable emission spectra, photostability, and high efficiency ideal for fluorescent imaging. 12-14 Superparamagnetic iron oxide nanoparticles are good contrast agents for magnetic resonance imaging. 15,16 Silica nanoparticles have a high acoustic impedance mismatch and can improve ultrasound imaging. Despite this success, one major limitation of most inorganic nanomaterials is no/slow biodegradability and high toxicity resulting from the long-term retention. 18-22 Therefore, biodegradation into non-toxic and renal clearable components is an ideal property of theranostic nanomaterials.^{23–2}

Metal oxide-doped phosphate (MODP) is an emerging class of biomaterials. MODP can be crystalline or non-crystalline. Crystalline MODP nanomaterials, for example, calcium phosphate (CP) nanocrystals, can be easily prepared from the controlled precipitation of metal (e.g. Ca^{2+}) and $H(PO_4)^{2-}$

ions and show promising biomedical applications, for example, gene delivery to breast cancer with fluorescence imaging.²⁹⁻³¹ However, these CP nanocrystals are not degradable at the physiological pH (\sim 7.3), causing the long-term retention problem when applied at the physiological pH. Even though they can degrade at more acidic conditions (pH < 6), that is, within the endosome/lysosome (pH 6-4.5), the resulting over-concentrated ions within the cell can trigger the cell necrosis.³¹ On the other hand, amorphous MODP or phosphate-based glasses are known for excellent biodegradability and biocompatibility at both the physiological and acidic pH values.³² This degradability is a result of their amorphous structure, that is, the terminal oxygen in the PO₄³⁻ tetrahedron reduces the connectivity of the phosphate network. After degradation, they release ions routinely found in the human body (e.g., PO₄³⁻, Ca²⁺, and Na⁺).³³ Finally,

Received: March 22, 2022 Revised: July 17, 2022 Published: August 5, 2022





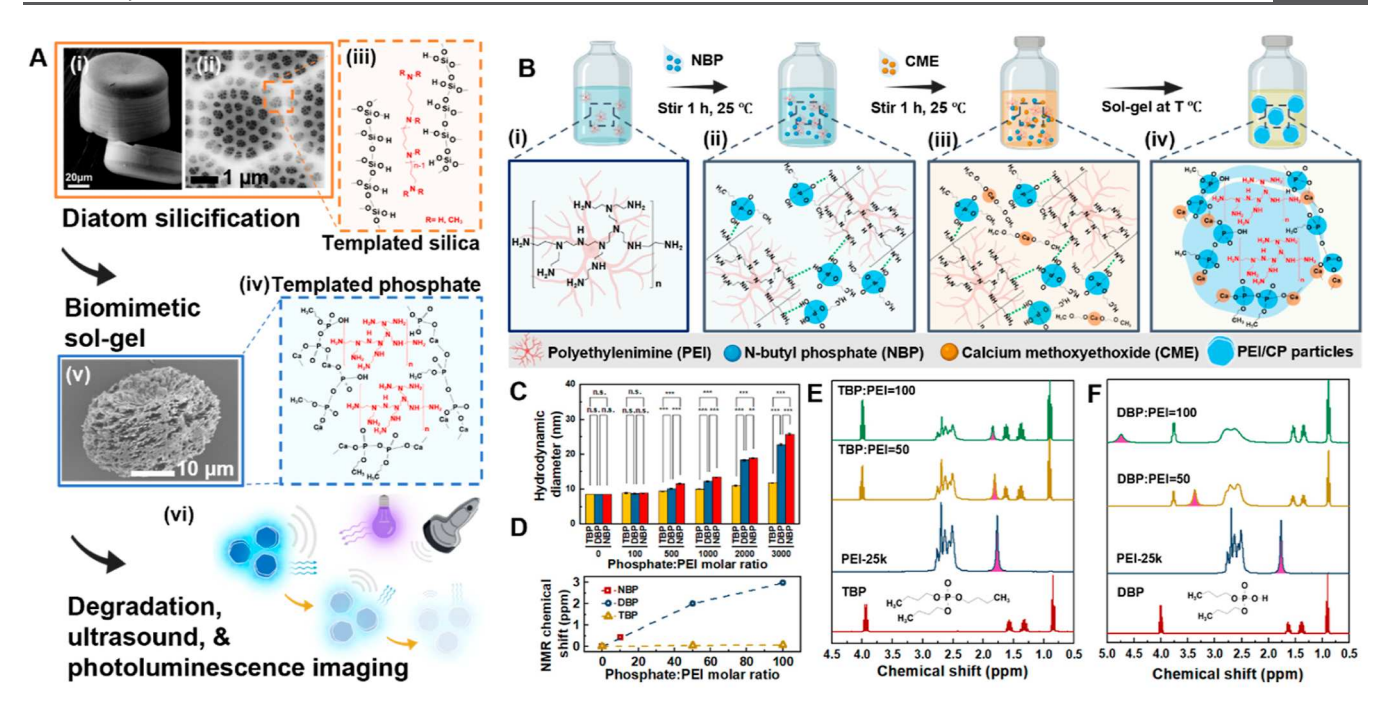


Figure 1. Diatom-inspired synthesis of PEI/CP for transient ultrasound and photoluminescence imaging. SEM images showing the [A(i)] diatom cell (coscinodiscus) and [A(ii)] silica cell wall made from the [A(iii)] biosilicification process, where silicic acids are templated by long-chain polyamine via hydrogen bonding between amine and hydroxyl groups and polycondense to form patterned silica. Peproduced with permission from Sumper and Kröger. Copyright (2004) Royal Society of Chemistry. [A(iv)] Scheme showing that by mimicking the biosilicification, phosphate precursors can also be templated by PEI, and further the reaction between phosphate and calcium precursors produces PEI/CP. [A(v)] SEM image showing an example of the as-prepared PEI/CP structure (PEI/CP-3). [A(v)] Scheme showing the biodegradation and decay of the ultrasound and photoluminescence signal of PEI/CP in water. Created with BioRender.com. (B) Synthesis simply adding n-butyl phosphate (NBP) to [B(i)] PEI in ethanol to form [B(ii)] templated PEI/NBP aggregates. These aggregates serve as nuclei in [B(iii)] the sol-gel reaction between calcium methoxyethoxide (CME) and NBP to form [B(iv)] PEI/CPs particles. Created with BioRender.com. (C) Hydrodynamic diameter of PEI/phosphate aggregates versus the phosphate/PEI molar ratio as measured by DLS showing that the aggregate size increases only with phosphate esters containing hydroxyl groups (DBP and NBP). In solution NMR spectra of PEI-25k (1 mM) and its mixture with (E) TBP and (F) DBP. 300 MHz, CDCl₃, 298 K. The amine peak of PEI (1.8 ppm) H is filled in pink.

phosphate glasses can be facilely functionalized by incorporating imaging dyes³⁴ and drugs.^{35,36} However, an obstacle to the wide theranostic application of phosphate glasses is the lack of facile, mild, and solution-based methods for preparing this material into monodispersed particles with controllable sizes. Ideally, the size should be tunable from nanometers to microns for customized theranostic tasks. Taking ultrasound imaging as an example, the pore size of tumor endothelium constrains the size of contrast agents to less than 380 nm for tumor targeting;³⁷ cell labeling requires the contrasts to be sufficiently small for efficient cell uptake. 17 However, for vascular imaging, contrasts of several microns (comparable to those of blood cells, e.g., microbubbles) are more suitable considering stronger echogenicity. 38,39 Phosphate glass particles (PGPs) of 200 nm $-3~\mu m$ have been prepared via sol-gel combined with electrospray. 34,40,41 These PGPs show strong echogenicity effective in in vivo ultrasound imaging and ease in incorporating dyes for fluorescence imaging. Moreover, their biodegradability and biocompatibility circumvent the longterm toxicity issue.³⁴ However, this synthetic approach is limited by sophisticated instrumentation, risk of electric shock (20-30 kV), and high temperature (180 °C) incompatible with temperature-sensitive drugs, peptides, and proteins. 40,41

One may learn from biosilicification in order to design a solution-based method for preparing phosphate glass micro-/

nano-particles. Diatoms are unicellular photosynthetic organisms known for the sophisticated design of their silica-based cell walls via the biosilicification process. ^{5,42,43,45} In this process, silicic acids are attracted and templated by aminerich polypeptides (silaffins) or long-chain polyamines via hydrogen bonding between the hydroxyl and amine groups. The templated silicic acid further polycondensates to form biosilica. ^{42,45} We hypothesized that a similar interaction could happen between phosphate precursors and synthetic polyamines [e.g., polyethylenimine (PEI)], which may be exploited to produce phosphate micro-/nano-particles.

Here, we report for the first time the synthesis of biodegradable PEI/CP micro-/nano composites via the biomimetic route for transient ultrasound and photoluminescence imaging. Inspired by the biosilicification process of diatoms, we applied PEI to template phosphate esters in solution and eventually produced PEI/CP particles with controllable size and morphology at a mild temperature range (25–90 °C). The interaction between phosphate precursors and PEI was systematically studied by dynamic light scattering (DLS) and ¹H solution nuclear magnetic resonance (NMR), confirming the formation of PEI/phosphate aggregates referred to as "phosphate sponges". These phosphate sponges act as nuclei and mediate the growth of PEI/CP particles. The size, morphology, composition, and

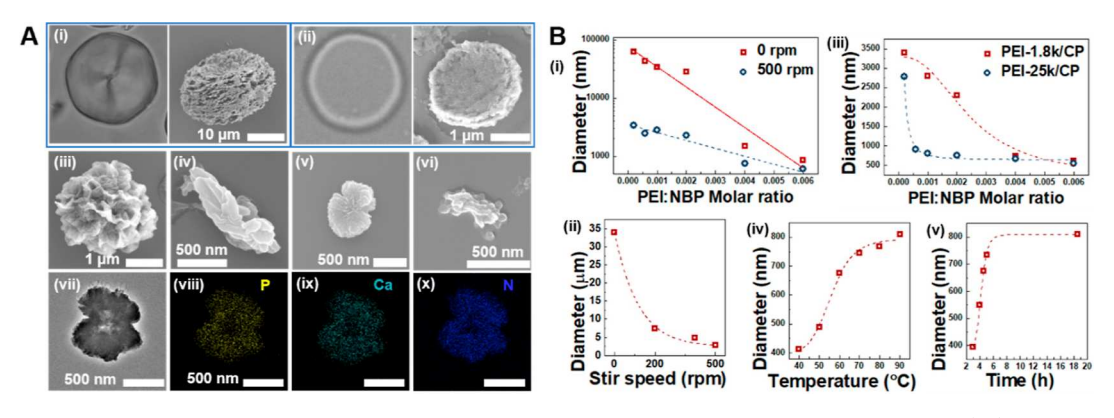


Figure 2. Exemplar particles and effects of synthetic parameters. Optical microscopy and SEM images showing [A(i,ii)] hexagonal micro-discs (PEI/CP-3 and -10), [A(iii)] micro-flower (PEI/CP-5), [A(iv)] micro-leaf (PEI/CP-25), [A(v)] nano-butterfly (PEI/CP-17), and [A(vi)] nanoribbon (PEI/CP-22). [A(vii-x)] TEM and EDX mapping images of the nano-butterfly (PEI/CP-17) showing element P, Ca, and N. The diameter decreases with increasing [B(i,ii)] PEI/NBP molar ratio, stirring speed, and [B(iii)] PEI molecular weight, while increases with increasing [B(iv)] reaction temperature and [B(v)] time.

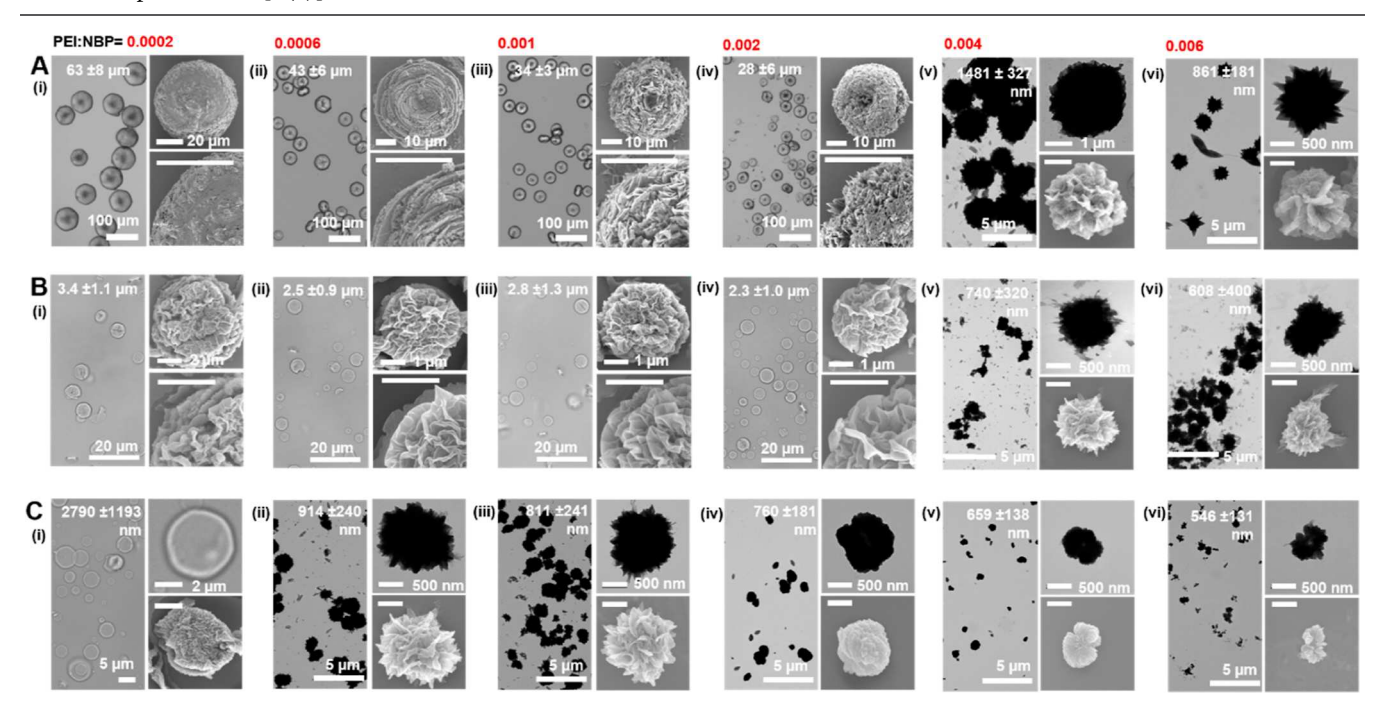


Figure 3. Effects of the PEI/NBP molar ratio, magnetic stirring, and PEI molecular weight. Optical microscopy (white, low-magnification), SEM (white, high-magnification), and TEM (black) images of PEI/CP prepared from (A) PEI-1.8k, 90 °C, 18.5 h, no stirring, and various PEI/NBP molar ratios (PEI/CP-1 to -6), (B) PEI-1.8k, 90 °C, 18.5 h, 500 rpm stirring, and various PEI/NBP molar ratios (PEI/CP-7 to -12), and (C) PEI-25k, 90 °C, 18.5 h, 500 rpm stirring, and various PEI/NBP molar ratios (PEI/CP-13 to -18).

chemical structure were characterized using DLS, SEM, transmission electron microscopy (TEM), optical microscopy, inductively coupled plasma mass spectroscopy (ICP–MS), energy-dispersive X-ray spectroscopy (EDX), Fourier transform infrared spectroscopy (FTIR), X-ray diffraction (XRD), and solid-state ³¹P and ¹H magic angle spinning nuclear magnetic resonance (MAS NMR). Lastly, their biodegradability, cell cytotoxicity, and promise for transient ultrasound and photoluminescence imaging was validated.

■ RESULTS AND DISCUSSION

Synthetic Strategy and Mechanism. We hypothesized that the hydroxyl-amine hydrogen bonding between silicic acid and polyamines found in diatoms (Figure 1A(i-iii))^{42,43} could also form between the phosphate precursor and synthetic PEI. This interaction may result in a templated phosphate precursor

(Figure 1A(iv)) and be exploited to produce structured PEI/CP micro-/nano-composites (Figure 1A(v)). Besides, these PEI/CP may be degraded in the aqueous environment and used as transient ultrasound and photoluminescence imaging agents (Figure 1A(vi)).

The synthesis (Figure 1B) simply added NBP and CME stepwise to branched PEI in ethanol. Ethanol was used instead of water to avoid the uncontrollable hydrolysis of CME. ³²,46 Then, the sol–gel reaction between NBP and CME was allowed at the controlled stirring rate (0–500 rpm), temperature (25–90 °C), and time (1–18.5 h) (see Methods and Table S1 for detailed parameters). NBP was chosen as the phosphate precursor because of its well-known reactivity with CME. ³² Mixing PEI and NBP may form PEI/NBP aggregates with reactive NBP on the surface via the hydrogen bonding between the hydroxyl group (NBP) and amine group (PEI)

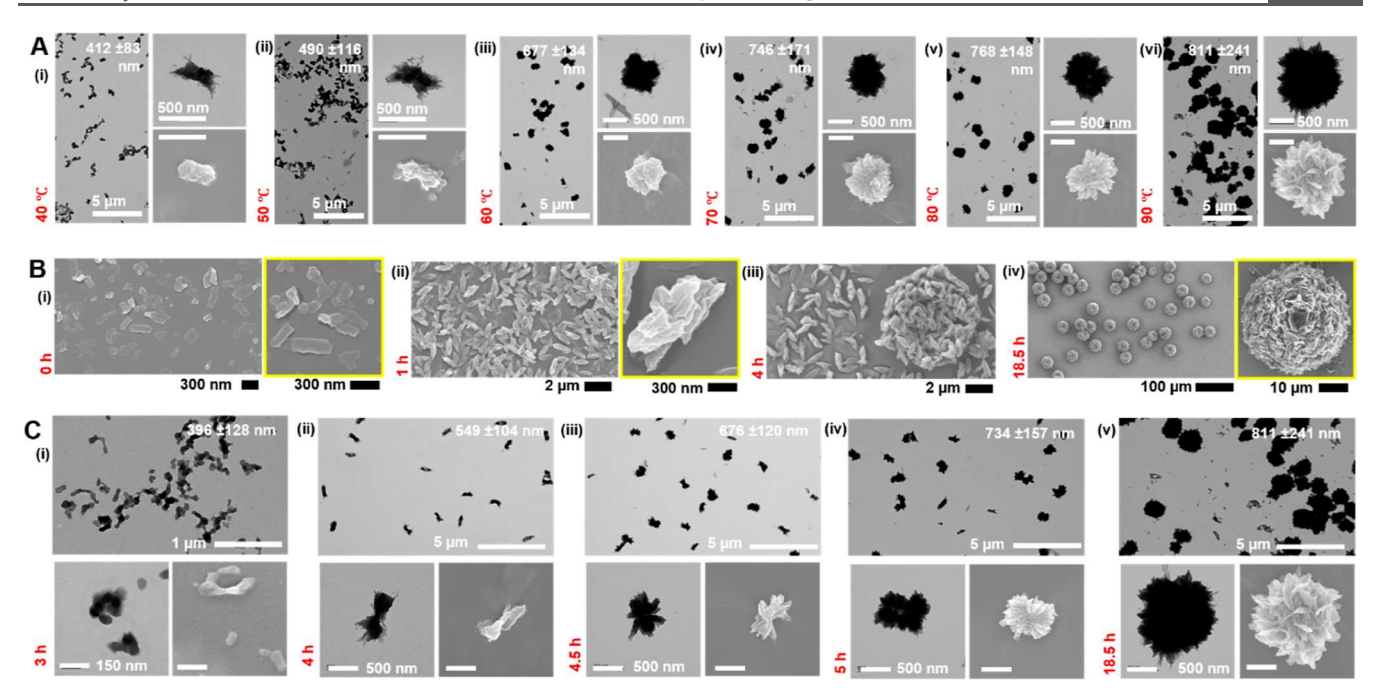


Figure 4. Effects of the reaction temperature and time. SEM (white) and TEM (black) images of PEI/CP prepared from (A) PEI-25k, PEI/NBP molar ratio 0.001, 90 °C, 18.5 h, 500 rpm stirring, and various temperatures: [A(i)] 40 °C (PEI/CP-23), [A(ii)] 50 °C (PEI/CP-22), A(iii) 60 °C (PEI/CP-21), [A(iv)] 70 °C (PEI/CP-20), [A(v)] 80 °C (PEI/CP-19), and [A(vi)] 90 °C (PEI/CP-15). The growth process of (B) hexagonal micro-disc (PEI/CP-3) and (C) nano-flower (PEI/CP-15).

(Figure 1B(ii)). We term these aggregates as "phosphate sponges" in analogy to the well-known "proton sponges". ⁴⁷ Upon the addition of CME (Figure 1B(iii)), it may react with NBP on the phosphate sponge surface (via hydrolysis and polycondensation) to form PEI/CP micro-/nano-composites (Figure 1B(iv)).

To verify the as-proposed phosphate sponge mechanism, the interaction between phosphate esters and branched PEI of 25k MW was studied using DLS (Figures 1C and S1) and ¹H solution NMR (Figures 1D-F and S2). TBP, DBP, and NBP are phosphate esters with 0, 1, and 1.5 equivalent hydroxyl groups on average (Figure S1A). In DLS measurements, ethanol was used to maintain the same solvent conditions as the synthesis process. DLS results showed a nearly invariant PEI hydrodynamic diameter (~10 nm) in the presence of increasing TBP (Figures 1C and S1B). However, a steady increment of the diameter was observed with increasing DBP and NBP addition (Figures 1C and S1C,D), indicating that the formation of PEI/phosphate aggregates is only possible when the phosphate precursor contains hydroxyl groups. To further prove that the formation of PEI/phosphate aggregates is governed by the hydrogen bonding between hydroxyl and amine groups, the chemical shift of the amine groups (PEI) was tracked by ¹H solution NMR when PEI was titrated by these phosphate esters (Figures 1D-F and S2). CDCl3 was used as the solvent to exclude the hydroxyl groups from the solvent. The amine peak of PEI (1.8 ppm, 44 highlighted in pink, Figure 1E) remained invariant, despite increasing TBP addition. However, in cases of both the DBP and NBP addition, the amine peak shifts steadily toward the downfield direction (Figures 1F and S2). Therefore, both DLS and ¹H solution NMR results support the formation of the phosphate sponges via hydrogen bonding between hydroxyl and amine groups.

Exemplar Particles, Composition, and Chemical Structure. This PEI-mediated sol—gel approach is simple (stepwise addition of reactants and incubation) and mild (25—90 °C). Moreover, it is highly flexible in controlling PEI/CP morphology (Figure 2A) and size (Figure 2B) when parameters were tuned. These parameters include the PEI/NBP molar ratio, solution dynamic conditions, PEI molecular weight, reaction temperature, and reaction time (see Table S1 for detailed parameters). The effects of these parameters will be discussed in detail later (Figures 3 and 4). Briefly, PEI/CP particles ranging from 63 \pm 8 μ m to 396 \pm 128 nm and versatile morphologies were obtained, including hexagonal micro-disc (Figure 2A(i,ii)), micro-flower (Figure 2A(iii)), micro-leaf (Figure 2A(iv)), nano-butterfly (Figure 2A(v)), and nano-ribbon (Figure 2A(vi)).

We expected the as-prepared particles to be composites of PEI and CP phases. The composite nature was proved using three tools. First, EDX mapping shows three major elements: P, Ca, and N (Figure 2A(vii-x)). Second, FTIR spectra of seven representative PEI/CP (Figure S3) show characteristic bands of PEI and phosphate species. Specifically, bands of PEI were seen at 2952-2862 and 1453 cm⁻¹ (CH₂CH₂), 1620-1585 cm⁻¹ (NH), and 1122 cm⁻¹ (CN). The phosphate phase was evidenced by bands at 1220 cm⁻¹ ($\nu_{as}(PO_2)^-$), 1000 and 1070 cm⁻¹ ($\nu_{as}(PO_3)^{2-}$), 900 cm⁻¹ ($\nu_{s}(P-O-P)$), and 790, 730, and 540 cm⁻¹ (δ (P-O-P)). Lastly, solid-state ³¹P and ¹H MAS NMR shows the presence of phosphate species and amine groups (Figure S5 and Table S3). The calculation of the composition based on ICP-MS (Table S2) showed that the weight percentage of PEI (or CP) varies from 67.34 (32.66%) to 50.26 (49.74%), depending on synthetic conditions. Besides, the CP phase has a formula of $(P_2O_5)_x(CaO)_{1-x}$, with x varying from 0.31 to 0.40.

XRD spectra of PEI/CP (Figure S4) were compared to those of nine typical CP phases reported in the litera-

ture. $^{40,50-57}$ The major XRD peaks of PEI/CP formed from PEI-25k match well with those of the HAp crystal 57 but are broader; PEI/CP prepared from PEI-1.8k have an even broader XRD pattern like the amorphous electrospray CP, 40 indicating the glassy nature of PEI/CP. Based on the broadness of XRD peaks, the degree of crystallization decreases in the order of HAp > PEI-25k/CP > PEI-1.8k/CP > electrospray CP.

There are three possible bonding types contributing to the PEI/CP network formation: P-O-P bonding, PO-Ca-OP bonding, and/or POH-NH2 hydrogen bonding. We first investigated the nature of P-O-P bonding using solid-state ³¹P MAS NMR. Qⁿ is widely applied to represent phosphate species, where n is the number of P-O-P bonding (i.e., bridging oxygens) in each PO₄³⁻ tetrahedron.³² For PEI/CP prepared from both PEI-1.8k and -25k, all ³¹P resonances (Figure S5 and Table S3) were observed between -4 and 4 ppm, which can be assigned to the Q1 speciation (i.e., pyrophosphate).⁵⁸ Therefore, pyrophosphate is the building block of PEI/CP. Figure S5I shows the chemical structure of pyrophosphate with four isolated oxygens highlighted. Assuming the presence of calcium oxide and partially reacted NBP, each of the four isolated oxygens can form PO-Ca, PO-H, or PO-CH₂CH₂CH₂CH₃ groups. Pyrophosphate units containing different combinations of these chemical groups are different Q¹ species measured by ³¹P MAS NMR (Figure S5). We observed only one dominant Q1 peak (~1 ppm) in all PEI-25k/CP (Figure S5D-H) and those prepared from a high PEI-1.8k concentration (Figure S5C). Pyrophosphate units in these PEI/CP are mainly connected by PO-Ca-OP because their ICP-MS-measured composition (Table S2) is close to $(P_2O_5)_{0.33}(CaO)_{0.67}$, which is the theoretical composition of the Q¹ species saturated by Ca. In contrast, multiple Q¹ species were seen from PEI/CP prepared from low PEI-1.8k concentrations (Figure S5A,B). Besides, the ICP-MSmeasured P₂O₅ ratio of these particles is larger than 0.33. Both results support the presence of PO-H and/or PO-CH2CH2CH3 along with PO-Ca. PO-H may form hydrogen bonding with NH2 (PEI) and therefore, further connects pyrophosphate units and extends the network. Indeed, solid-state¹H MAS NMR results (Figure S5A,B) of PEI/CP containing multiple Q¹ species also show multiple amine peaks, including those highly shifted (>9 ppm), which supports the formation of POH-NH2 hydrogen bonding.

Effects of the PEI/NBP Molar Ratio. Sol-gel reactions were first performed using PEI-1.8k at 90 °C for 18.5 h without magnetic stirring. The PEI/NBP molar ratio was varied from 0.0002 to 0.006. The average diameter of PEI/CP decreases as the molar ratio increases and can be tuned from 63 \pm 8 μ m (ratio = 0.0002) to 861 nm (ratio = 0.006) (Figures 2B(i) and 3A. See Figure S6 for size distributions). PEI/CP appeared to be porous hexagonal micro-discs with the size ranging from 28 \pm 6 to 63 \pm 8 μ m when the molar ratio was between 0.0002 and 0.002 (Figures 2A(i) and 3A(i-iv)). High-magnification SEM images (Figure 3A(i-iv)) indicate that these hexagonal micro-discs may be assembled from smaller micro-flakes, which is supported by particle growth studies shown later (Figure 4B). This PEI/NBP molar ratio-dependent size change can be explained by the proposed phosphate sponge mechanism. Phosphate sponges can be considered as nuclei for particle growth. With fixed NBP and CME addition, a higher PEI/NBP molar ratio results in a higher number-concentration of nuclei and therefore smaller particles.

Effects of Solution Dynamic Conditions. We then repeated sol–gel reactions using PEI-1.8k at 90 °C for 18.5 h with magnetic stirring at 500 rpm. At the same PEI/NBP molar ratio, magnetic stirring at 500 rpm resulted in 18.5 to 1.4 times smaller particles than without stirring (Figure 2B(i)). These particles also appeared to be micro-discs with the molar ratio ranging from 0.0002 to 0.002 (Figure 3B(i–iv)) and micro-/nano-flowers when the ratio was above 0.002 (Figure 3B(v,vi)). By carefully controlling the stirring speed from 0 to 200, 400, and 500 rpm, the average particle size can be finely tuned from 34 \pm 3 to 7.8 \pm 2.7, 4.8 \pm 1.4, and 2.8 \pm 1.3 μ m (Figures S6C and S7).

Effects of the PEI Molecular Weight. To determine the influence of the PEI molecular weight, PEI-1.8k was replaced by either PEI-25k or PEI-800, while other conditions were kept the same (Figure 3C). Comparing Figure 3C to B, at the same PEI/NBP molar ratio, PEI-25k resulted in smaller particles. This trend is clearer in Figure 2B(iii). The micro-disc shape (~2790 nm) appeared when the molar ratio was 0.0002 (Figure 3C(i)). When the molar ratio exceeded 0.0002, submicron-flowers (914 \pm 240 to 760 \pm 181 nm) and nanobutterflies (659 \pm 138 to 546 \pm 131 nm) were formed (Figure 3C(ii-vi)). The PEI molecular weight-dependent size change can be explained by the difference in chemical bonding. Based on the solid-state 31P and 1H MAS NMR results discussed before (Figure S5 and Table S3), PEI/CP prepared from lowconcentration PEI-1.8k can extend their network via both PO-Ca-OP and POH-NH₂ hydrogen bonding, which explains for the formation of larger particles in these conditions. However, in the case of high-concentration PEI-1.8k and PEI-25k, the connection of pyrophosphate units via the POH-NH2 hydrogen bonding is less likely, resulting in smaller particles. As shown in Figure S8, within the tested range of PEI/NBP molar ratio (0.0002 to 0.006), PEI-800 did not produce monodispersed particles with defined shapes as seen in the case of PEI-1.8k and PEI-25k. Instead, only amorphous gel-like products were observed. This difference indicates that PEI-800 may be too small to efficiently regulate the growth of monodispersed PEI/CP particles.

Effects of the Reaction Temperature. Sol-gel reactions were also carried out at various temperatures (90, 80, 70, 60, 50, and 40 °C) with other parameters being kept constant (PEI-25k/NBP = 0.001, magnetic stirring at 500 rpm, and 18.5 h). The average diameter of particles increased as the reaction temperature was raised (Figures 2B(iv) and 4A). At 40 and 50 °C, particles have a nano-ribbon morphology (490 and 412 nm) (Figure 4A(i,ii)). When the temperature was adjusted between 60 and 90 °C, particles possess the nano-flower morphology (from 811 \pm 241 to 768 \pm 148, 746 \pm 171, and 677 \pm 134 nm) (Figure 4A(iii,iv)). The temperature-dependent change of the particle size can be explained by the reaction kinetics. A higher reaction temperature may result in faster reaction and particle growth and therefore a larger size during a given period of the reaction.

Effects of the Reaction Time. The hexagonal micro-disc (PEI/CP-3) and nano-flower (PEI/CP-15) were chosen as models to understand the growth of PEI/CP particles. Particles were collected at different time points and examined. Figure 4B shows the evolution of the hexagonal micro-disc (PEI/CP-3) over time. The first hour of the reaction at room temperature resulted in an inhomogeneous mixture of nano-spheres (\sim 80 nm) and nano-rods ($L \times W = 400 \times 150$ nm, Figure 4B(i)). After raising the temperature to 90 °C for another hour, these

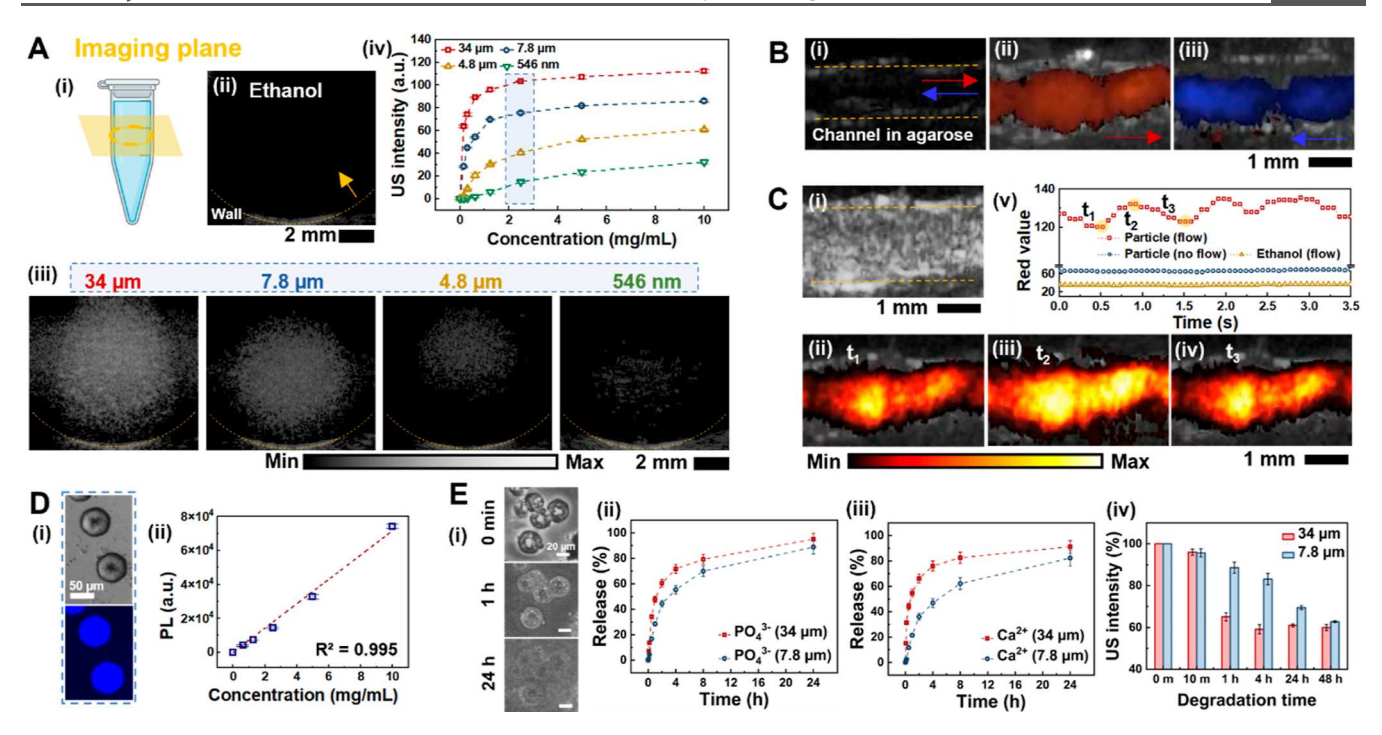


Figure 5. Ultrasound and photoluminescence imaging and biodegradability. (A) B-mode imaging. [A(i)] Imaging slice in a tube. B-mode images of [A(ii)] ethanol and [A(iii)] 2.5 mg/mL ethanol solution of PEI/CP-3 (34 \pm 3 μ m), PEI/CP-31 (7.8 \pm 2.7 μ m), PEI/CP-32 (4.8 \pm 1.4 μ m), and PEI/CP-18 (546 \pm 131 nm). Dashed lines and arrow show the tube wall. [A(v)] Ultrasound intensity versus the particle concentration. (B,C) Doppler imaging. Overlap of color Doppler and B-mode images when flowing [B(i)] water and [B(ii,iii)] 10 mg/mL PEI/CP-31 (7.8 \pm 2.7 μ m) in ethanol. Overlap of power Doppler and B-mode images of 10 mg/mL PEI/CP-31 (7.8 \pm 2.7 μ m) in ethanol [C(i)] without and [C(ii–iv)] with flow at time points marked in [C(v)]. [C(v)] Doppler intensity versus time. (D) Photoluminescence imaging. [D(i)] Fluorescence microscopy images showing PEI/CP-3 emitting blue light [4',6-diamidino-2-phenylindole (DAPI), excitation at 358 nm]. [D(ii)] Photoluminescence intensity vs the PEI/CP-3 concentration (excitation at 350 nm). (E) Biodegradability. [E(i)] Optical microscopy images showing the dissolution of PEI/CP-3 under a continuous flow of PBS. [E(ii,iii)] Release of PO₄³⁻ and Ca²⁺ from PEI/CP-3 under a continuous flow of fresh water (pH 7.30). [E(iv)] Decay of the ultrasound intensity when PEI/CP-3 and -31 degrade (2.5 mg/mL in 1:1 ethanol and PBS buffer).

mixed structures transformed into homogenous micro-leaves $(L \times W = 1200 \times 400 \text{ nm}, \text{ Figure 4B(ii)})$. While extending the reaction time at 90 °C to 4 h (Figure 4B(iii)), the size and shape of micro-leaves remained almost the same; meanwhile, parts of these micro-leaves assembled to form a loose microdisc structure (\sim 7 μ m in diameter), implying the transition from micro-leaf growth to the assembly during this period. Finally, when the reaction time at 90 °C reached 18.5 h, microleaves disappeared, and larger and homogeneous hexagonal micro-discs (34 \pm 3 μ m in diameter) were observed (Figure 4B(iv)). In short, the formation of hexagonal micro-discs started with the growth of micro-leaves from a mixture of nano-spheres and nano-rods. The as-formed micro-leaves then assembled to form the loose micro-disc structure. Finally, further deposition of materials on the micro-disc surface led to the formation of larger and denser hexagonal micro-discs.

A similar observation was obtained for nano-flowers (PEI/CP-15, Figure 4C). The growth of PEI/CP-15 also began with a mixture of nano-spheres and nano-rods with an average diameter of 396 ± 128 nm (3 h at 90 °C, Figure 4C(i)). After 4 h at 90 °C, these mixed particles transformed into homogenous nano-ribbons (549 ± 104 nm, Figure 4C(ii)). These nano-ribbons then evolved into nano-flowers with the size increasing from 676 ± 120 nm (4.5 h at 90 °C, Figure 4C(iii)) to 734 ± 157 nm (5 h at 90 °C, Figure 4C(iv)) and 811 ± 241 nm (18.5 h at 90 °C, Figure 4C(v)) (see Figure 28(v) for the diameter vs time relationship).

Ultrasound and Photoluminescence Imaging. We hypothesized that PEI/CP particles can have a high acoustic

impedance mismatch with the liquid phase and be used as ultrasound contrasts. To determine how the particle size and concentration affect the echogenicity, PEI/CP in ethanol solution were added to tubes (Figure 5A(i)) and imaged in the B-mode at 18 MHz. Ethanol was used as the solvent at this step to prevent any uncertainties from the degradation caused by water. No ultrasound signal was detected from pure ethanol (Figure 5A(ii)). At the same particle mass concentration (2.5 mg/mL), the ultrasound intensity increases with increasing particle size (546 \pm 131 nm to 34 \pm 3 μ m, Figure 5A(iii)), which is consistent with previous findings and can be attributed to the differences in the scattering cross-section. 59,60 This size effect holds true for all concentrations tested (0-10)mg/mL, Figure 5A(iv)). With a given size, the ultrasound signal increases as the mass concentration increases (Figure 5A(iv)). A linear intensity-concentration relationship was seen at the lower concentration range (Figure S9). Defining the limit of detection (LOD) as the concentration of particles creating the intensity at three standard deviations above the mean of the background and using a background value of 0.08 \pm 0.01 and the best-fit equations (Figure S8), we estimated the LOD of PEI/CP of 34 \pm 3 μ m, 7.8 \pm 2.7 μ m, 4.8 \pm 1.4 μ m, and 546 \pm 131 nm to be 0.17, 0.30, 1.47, and 11.10 μ g/mL, respectively. The LOD of 546 \pm 131 nm PEI/CP is comparable with that reported for silica NPs (18.5 μ g/mL, 300 nm, at 16 MHz), which has been demonstrated as feasible for in-vivo stem cell imaging.1

Contrasts with size comparable to that of blood cells have been used for Doppler vascular imaging. ^{38,39} Here, we tested in

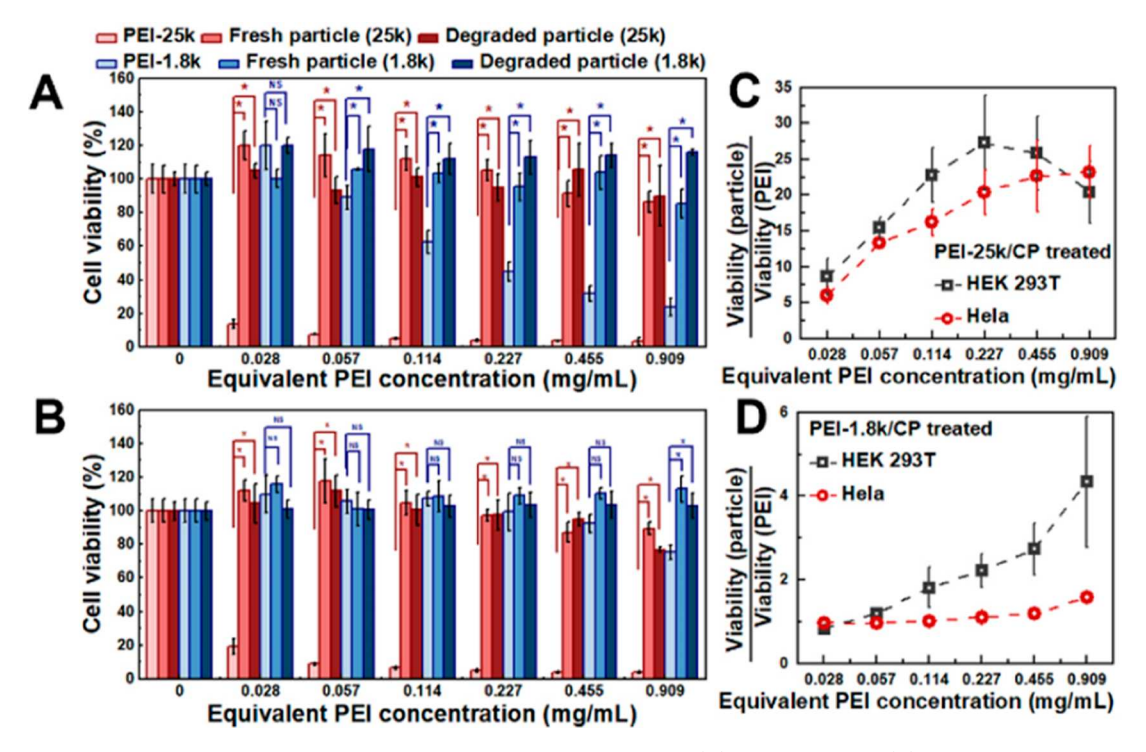


Figure 6. Cell cytotoxicity of pristine PEI and PEI/CP. Tests used resazurin assay on (A) HEK 293T and (B) HeLa cells. The ratio of viability of cells treated with fresh particles to that of pristine PEI in the case of (C) PEI-25k and (D) PEI-1.8k. PEI/CP-5 was selected to represent particles made from PEI-1.8k and PEI/CP-15 for PEI-25k. PEI/CP shows negligible cytotoxicity compared to pristine PEI. *: $p \le 0.05$; NS: not significant, that is, p > 0.05; n = 4.

vitro the potential of using PEI/CP for Doppler imaging. As a negative control, pure ethanol was constantly pumped through a channel inside an agarose phantom using a peristaltic pump, which did not result in detectable color-Doppler signals (Figure 5B(i)). In contrast, flowing 10 mg/mL PEI/CP-31 (7.8 μ m) generated color-Doppler signals with recognizable flow directions (red or blue, Figure 5B(ii,iii)). The power-Doppler mode is used clinically to monitor heartbeat and changes in the blood flow rate. Taking advantage of the pulsive flow of the peristaltic pump, we were able to mimic the heartbeat. Heartbeat-like wavy power-Doppler signals were observed from the flow of PEI/CP-31 but not ethanol or stagnant particles (Figure 5C).

PEI/CP also emitted blue light when excited at 358 nm (Figure 5D(i)). This is due to the intrinsic photoluminescence of PEI reported previously, although the mechanism of this intrinsic photoluminescence is yet to be explored.⁶¹ The emission peaks of pure PEI-1.8k and PEI/CP were found at 411 and 450 nm (excitation at 350 nm, Figure S10).

The photoluminescence intensity increases linearly with the PEI/CP concentration (Figure 5D(ii)). Although, considering the low quantum yield (1%) reported for PEI-1.8k and PEI-25k, FEI/CP may not be the best choice for fluorophores, this intrinsic photoluminescence can still be used for labeling and tracking these particles when necessary.

Degradability. The poor clearance of nanomaterials is a major impediment to clinical translation. By design, PEI/CP should slowly degrade into small molecules and simple ions for renal clearance. We further tested the degradability of PEI/CP. Optical microscopy images show that PEI/CP gradually dissolved in PBS buffer (Figure 5E(i)). PEI/CP particles were continuously hydrated by fresh water (pH 7.30) and a release of about 80–90% major ions (i.e., PO₄³⁻ and Ca²⁺)

were detected within the first 24 h, using ICP–MS (Figure 5E(ii,iii)). When dissolving PEI/CP in a static PBS buffer, the ultrasound intensity dropped about 40% within the first 24 h and only slightly in the next 24 h (Figure 5E(iv)). Therefore, in practice, PEI/CP can be dispersed in PBS buffer and used as transient ultrasound contrast agents with a 24 h imaging window. They may bridge the gap between the unstable gas microbubbles (degrade within 30 min) 17 and slowly-degradable silica nanoparticles (degrade after 24 days),⁶² considering the degradation speed.

Cell Cytotoxicity. The dose-dependent cytotoxicity of pure PEI and PEI/CP composites was evaluated with HEK 293T and HeLa cells, using the resazurin assay (Figure 6). Pure PEI-25k showed high cytotoxicity; a low dose of 0.028 mg/mL can dramatically reduce the cell viability to below 20%. PEI-1.8k is less toxic but still caused a steady drop in the viability of HEK 293T (Figure 6A). Surprisingly, PEI/CP has negligible cytotoxicity compared to PEI. Both cell types treated with fresh and degraded PEI-25k/CP and PEI-1.8k/CP have viability above 85% in the concentration range tested, except HeLa cells treated with 0.909 mg/mL degraded PEI-25k/CPs (77%). In the case of HEK 293T cells, fresh PEI-25k/CP and PEI-1.8k/CP, respectively, resulted in 9-26 and 1-4 times, respectively, higher viability than the corresponding PEI; these values are 6-23 and 1-1.6 in the case of HeLa cells (Figure 6C,D). The toxicity of pure PEI is originated from the damage of the cell membrane by abundant positive amine groups. 63 Therefore, the reduced cytotoxicity of PEI/CP compared to pure PEI can be explained by the charge neutralization by negative phosphate species in both intact and degraded phases.

CONCLUSIONS

We demonstrated a facile and mild (25-90 °C) synthesis mimicking the biosilicification in diatoms for preparing PEI/ CP composites. Using DLS and ¹H solution NMR, we proved the formation of proposed "phosphate sponges" which are aggregates composed of phosphate esters and PEI resulting from hydrogen bonding between hydroxyl (from phosphate ester) and amine groups (from PEI). These phosphate sponges served as nuclei in the reaction of CME and phosphate esters. By controlling parameters such as the PEI/NBP molar ratio, solution dynamic conditions, PEI molecular weight, reaction temperature, and reaction time, PEI/CP composites were prepared with versatile sizes (396 \pm 128 nm to 63 \pm 8 μ m) and morphologies (hexagonal micro-disc, micro-flower, microleaf, nano-butterfly, and nano-ribbon). PEI/CP exhibited excellent biocompatibility and biodegradability, indicated by negligible cell cytotoxicity and degradation within 24 h. The echogenicity of PEI/CP increases with the increment of size and concentration. PEI/CP also generated Doppler signals containing the flow direction and speed information. Finally, PEI/CP showed intrinsic blue photoluminescence. We envision that PEI/CP particles are promising transient ultrasound and photoluminescence imaging agents.

■ METHODS

Materials. Ethanol (200 proof, Koptec) and PBS (×1, Corning) were purchased from VWR. Tri-*n*-butyl phosphate (TBP, 98%) and branched PEI (b-PEI, 1.8k MW) were purchased from Alfa Aesar. NBP (a 1:1 mixture of mono-*n*-butyl and di-*n*-butyl) was purchased from Thermo Scientific. DBP (97.0%), b-PEI (25k and 800 MW), chloroform-*d* (CDCl₃, 99.8 atom % *D*), and resazurin were purchased from Sigma-Aldrich. CME (20% in methoxyethanol) was purchased from ABCR Chemical. Ultrapure agarose (Invitrogen) was purchased from Fisher Scientific.

Synthesis of PEI/CP. Ethanol was used instead of water to avoid the uncontrollable hydrolysis of CME. 32,46 bPEI (MW 1.8k or 25k) was dissolved in ethanol to make a 1×10^{-5} mol/mL PEI stock solution. An appropriate amount of the PEI stock solution was then diluted by extra ethanol to make the desired final PEI concentration. Under magnetic stirring at 500 rpm, NBP was added to the diluted PEI in ethanol. After stirring at room temperature for 1 h, CME was added, and the solution was allowed for another 1 h stirring at room temperature. Then, the well-mixed solution was incubated at a raised temperature with or without magnetic stirring for a certain reaction time. All detailed parameters, including reagent addition, stirring speed, temperature, and reaction time can be found in Table S1. The as-prepared particles were purified by repeating centrifugation (5000 rpm, 20 min) and ethanol wash 3 times.

¹H Solution NMR and DLS Study of the Interaction between PEI and Phosphate Esters. The interaction between PEI and phosphate esters was studied with the combination of ¹H solution NMR and DLS. PEI (25k MW) was first dissolved in either CDCl₃ (for ¹H solution NMR) or ethanol (DLS) to make 1 mM PEI solution. Then, an appropriate amount of phosphate precursor (TBP, NBP, or DBP) was mixed with the PEI solution to obtain the desired phosphate/b-PEI molar ratios. ¹H solution NMR spectra were recorded on the Bruker 300 MHz spectrometer, and all chemical shifts are referenced to the reported literature ⁶⁴ (CDCl₃: 7.26 ppm). DLS measurements were performed on the Malvern NANO-ZS90 Zetasizer to determine hydrodynamic sizes of PEI/phosphate ester aggregates.

Morphology and Size of PEI/CP Particles. SEM images were obtained using the Zeiss Sigma 500 operated at 5 kV with a 30 μ m aperture and 10 mm working distance. Particles in ethanol were dropcoated on a silicon substrate (Ted Pella Inc), dried at room temperature, and sputter-coated with gold alloys before SEM. TEM images and EDX mapping images were acquired using the FEI Tecnai

F20 instrument at an operation voltage of 200 kV. Particles in ethanol were drop-coated on a copper TEM grid, and ethanol was evaporated naturally at room temperature before TEM imaging.

Keyence fluorescence microscope was used for observations of microparticles either in bright field mode or fluorescence mode (DAPI channel, excitation 358 nm). For characterizing the morphology, ethanol was used as the solvent. To monitor the particle degradation, particles were deposited in a flow cell, 65 and PBS was flowed at 1.2 mL/min to simulate the human blood flow. [See Figure S11 (Supporting Information) for details of the flow cell design]. DLS measurements were performed on the Malvern NANO-ZS90 Zetasizer to determine hydrodynamic sizes of both PEI/phosphate ester aggregates and PEI/CP particles (<1.5 μ m) dissolved in ethanol. The size distribution of PEI/CP particles larger than 1.5 μ m was determined by image analysis over 500 particles using Image-Pro Plus software, based on optical microscopy images.

Spectral Studies of the PEI/CP Particles. PEI/CP particles in ethanol were dried under vacuum at room temperature and used for spectral studies. FTIR spectroscopy was performed on the PerkinElmer spectrum two FTIR spectrometer. XRD was performed on the Rigaku MiniFlex with Cu K α radiation (λ = 1.5406 Å). Solidstate ³¹P and ¹H MAS NMR. All ³¹P MAS NMR measurements were performed at 9.4 T using the Bruker 400 MHz AVANCE III HD spectrometer operating at a Larmor frequency of 161.4 MHz (398.8 MHz for ¹H). Samples were loaded under a N₂ atmosphere into Bruker 3.2 mm rotors and spun at a magic angle spinning (MAS) frequency of 15 kHz. Each spectrum was acquired at room temperature by direct excitation (single pulse) methods employing $\pi/4$ pulses of length 2 μ s and 80 kHz of ¹H decoupling which was applied during data (FID) acquisition. To ensure quantitative results, a recycle delay of 300 s was used which was checked against tests of longer recycle delays. All data were referenced against the IUPACrecommended primary reference of 85% H_3PO_4 ($\delta_{iso} = 0.0$ ppm), via a secondary solid reference of ammonia dihydrogen phosphate ((NH₃)H₂PO₄ or ADP) (δ_{iso} = 0.99 ppm). The corresponding solidstate ¹H MAS NMR room temperature measurements were undertaken at 16.4 T using the Bruker 700 MHz AVANCE III HD spectrometer operating at a Larmor frequency of 700.13 MHz. All samples were packed under a N2 atmosphere into Bruker 1.3 mm rotors and spun at a MAS frequency of 60 kHz. To obtain quantitative spectra, direct excitation (single pulse) methods using $\pi/4$ pulses of length 1.25 μ s were used in conjunction with a recycle delay of 10 s. All data were referenced against the IUPAC-recommended primary reference of tetramethylsilane ((CH₃)₄Si) (δ_{iso} = 0.0 ppm), via a secondary solid reference using the methyl (CH₃) group resonance from alanine ($\delta_{\rm iso}$ = 1.1 ppm). The acquisition and processing of all solid-state NMR data were performed using the Bruker TopSpin software package, while deconvolution of spectra was performed using DMFit. Photoluminescence emission measurements were performed on the BioTek Synergy H1 microplate reader.

ICP–MS Measurements. ICP–MS measurements were carried out using iCAP RQ, Thermo Scientific. For ICP–MS analysis of the particle composition, overnight digestion of particles was carried out by adding 571 μ L of 70% nitric acid to 0.01 mg of dried particles in a glass vial. This solution was transferred to a 15 mL plastic centrifugation tube, and Millipore water was added to make a final solution of 10 mL. For ICP–MS analysis of particle ion releases, 0.1 mL of 10 mg/mL particle in ethanol was deposited on a syringe filter (Millex-GP, 220 nm). Millipore water (pH 7.30) was continuously pumped (1.2 mL/h) through the particle-loaded syringe filter. The solution was collected at the time points of 0, 5, 10, 30, 60, 120, 240, 480, and 1440 min. Collected solutions were diluted 100 times with 4% HNO₃ and measured by ICP–MS.

In Vitro Ultrasound Imaging. Ultrasound images were captured with the Verasonics, Vantage 256 system at 40 V with a L22-14vX transducer (18 MHz, 3k PRF, 6 pulse cycles, ~30% bandwidth, 128 elements, and 0.10 mm pitch). Ethanol solutions of PEI/CP-3 (34 \pm 3 μ m), PEI/CP-31 (7.8 \pm 2.7 μ m), PEI/CP-32 (4.8 \pm 1.4 μ m), and PEI/CP-18 (546 \pm 131 nm) from 0 to 10 mg/mL were loaded into a 1.5 mL plastic centrifuge tube. The tube was immersed in a water

bath, and B-mode ultrasound images were acquired. To determine the ultrasound intensity decay during the particle dissolution, PEI/CP-3 (34 μ m) and PEI/CP-31 (7.8 μ m) were dispersed in 1:1 ethanol, and PBS buffer solution with a final concentration of 2.5 mg/mL was used. The ultrasound intensity was then quantified by measuring the average RGB value of the same area of interest using ImageJ. For Doppler imaging, 10 mg/mL of PEI/CP-31 (7.8 μ m) in ethanol solution was pumped through a channel inside an agarose phantom (2 wt %) with a peristaltic pump. The average red value inside the area of interest was measured using ImageJ to quantify the power Doppler intensity.

Cell Cytotoxicity. The cytotoxicity of materials (pure PEI-1.8k, pure PEI-25k, fresh PEI/CP-5 and -15, and PEI/CP-5 and -15 degraded for 24 h in PBS) was studied on both HEK 293T and HeLa cells, using resazurin assay. 0.1 mL of cell solution [200,000 count/ mL in Dulbecco's modified Eagle medium (DMEM) with 10% fetal bovine serum and 1% PS was loaded on a 96-well plate and incubated for 24 h (5% CO₂ at 37 °C). 0.01 mL of materials in PBS buffer was added to wells containing cells in DMEM to make the final equivalent PEI concentration in the well in the range from 0 to 1 mg/ mL. After material addition, the cells were incubated for another 24 h (5% CO₂ at 37 °C). 0.01 mL of resazurin was then added to each well. After incubation for another 2 h, the fluorescence was read. A well with only DMEM and resazurin dyes and another well with only cells, DMEM, and resazurin dyes were also prepared, following the same volume and incubation conditions. In the case of PEI/CP particles, the equivalent PEI concentration is defined as the resulting PEI concentration, assuming a complete dissolution of PEI/CP particles. Therefore, to achieve the equivalent PEI concentration, higher PEI/CP mass concentration was used than pure PEI. The cell viability was calculated as follows

$$\text{cell viability} = \frac{\text{FL}_{\text{material}} - \text{FL}_{\text{empty}}}{\text{FL}_{\text{cell}} - \text{FL}_{\text{empty}}} \times 100\%$$

 $FL_{material}$: fluorescence intensity read from the well with cells, DMEM, resazurin dyes, and materials (PEI-1.8k, PEI-25k, fresh PEI/CPs, or PEI/CPs degraded for 24 h); FL_{empty} : fluorescence intensity read from the well with only DMEM and resazurin dyes; FL_{cell} : fluorescence intensity read from the well with only cells, DMEM, and resazurin dyes.

■ ASSOCIATED CONTENT

Supporting Information

The Supporting Information is available free of charge at https://pubs.acs.org/doi/10.1021/acs.chemmater.2c00857.

Synthetic parameters, composition (ICP–MS), DLS and ¹H solution NMR titration showing the formation of PEI/phosphate aggregates, FTIR, XRD, solid-state ³¹P and ¹H MAS NMR images, size distribution of PEI/CP particles, schematic illustration of the flow cell design for studying the degradability of particles, optical microscopy images, US intensity versus concentration, and photoluminescence emission spectra (PDF)

AUTHOR INFORMATION

Corresponding Author

Jesse V. Jokerst — Materials Science and Engineering Program,
University of California San Diego, La Jolla, California
92093, United States; Department of NanoEngineering,
University of California San Diego, La Jolla, California
92093, United States; Department of Radiology, University of
California San Diego, La Jolla, California 92093, United
States; □ orcid.org/0000-0003-2829-6408;
Email: jjokerst@ucsd.edu

Authors

Tengyu He — Materials Science and Engineering Program, University of California San Diego, La Jolla, California 92093, United States; oorcid.org/0000-0002-6767-4849

David G. Bradley – Department of Physics, University of Warwick, Coventry CV4 7AL, UK

Ming Xu − Department of NanoEngineering, University of California San Diego, La Jolla, California 92093, United States; ocid.org/0000-0002-6998-8462

Shu-Ting Ko – Materials Science and Engineering Program, University of California San Diego, La Jolla, California 92093, United States

Baiyan Qi – Materials Science and Engineering Program, University of California San Diego, La Jolla, California 92093, United States

Yi Li – Department of NanoEngineering, University of California San Diego, La Jolla, California 92093, United States

Yong Cheng – Department of NanoEngineering, University of California San Diego, La Jolla, California 92093, United States

Zhicheng Jin — Department of NanoEngineering, University of California San Diego, La Jolla, California 92093, United States; occid.org/0000-0001-6072-7533

Jiajing Zhou — Department of NanoEngineering, University of California San Diego, La Jolla, California 92093, United States; orcid.org/0000-0001-5203-4737

Lekshmi Sasi — Department of NanoEngineering, University of California San Diego, La Jolla, California 92093, United States

Lei Fu — Department of NanoEngineering, University of California San Diego, La Jolla, California 92093, United States

Zhuohong Wu – Department of NanoEngineering, University of California San Diego, La Jolla, California 92093, United States

Jingcheng Zhou — Department of NanoEngineering, University of California San Diego, La Jolla, California 92093, United States

Wonjun Yim — Materials Science and Engineering Program, University of California San Diego, La Jolla, California 92093, United States; © orcid.org/0000-0002-0242-7898

Yu-Ci Chang — Materials Science and Engineering Program, University of California San Diego, La Jolla, California 92093, United States; © orcid.org/0000-0001-6997-9884

John V. Hanna – Department of Physics, University of Warwick, Coventry CV4 7AL, UK; [®] orcid.org/0000-0002-0644-3932

Jian Luo – Materials Science and Engineering Program, University of California San Diego, La Jolla, California 92093, United States; Department of NanoEngineering, University of California San Diego, La Jolla, California 92093, United States

Complete contact information is available at: https://pubs.acs.org/10.1021/acs.chemmater.2c00857

Author Contributions

T.H. and J.V.J. conceived the idea. T.H. conducted the major material synthesis. All authors performed the general measurements. T.H. and J.V.J. drafted the manuscript. All authors have given approval to the final version of the manuscript.

Notes

The authors declare no competing financial interest.

ACKNOWLEDGMENTS

The authors acknowledge the support from the NSF funding under award 1845683 and NIH funding under award P30 NS047101. This work was performed in part at the San Diego Nanotechnology Infrastructure (SDNI) of University of California San Diego, a member of the National Nanotechnology Coordinated Infrastructure (NNCI), which is supported by the National Science Foundation (Grant ECCS-1542148). The authors acknowledge the use of facilities and instrumentation provided by NSF through the UC San Diego Materials Research Science and Engineering Center (UCSD MRSEC) (Grant DMR-2011924). S.-T.K. and J.L. acknowledge partial support from the NSF MRSEC program through the UC Irvine Center for Complex and Active Materials (DMR-2011967). J.V.H. acknowledges financial support for the solid-state NMR instrumentation at Warwick used in this research which was funded by the EPSRC (grants EP/M028186/1 and EP/K024418/1), the BBSRC, the University of Warwick, and the Birmingham Science City AM1 and AM2 projects which were supported by Advantage West Midlands (AWM) and the European Regional Development Fund (ERDF). Ultrasound imaging used infrastructure suppored by S10 OD021821.

REFERENCES

- (1) Weber, J.; Beard, P. C.; Bohndiek, S. E. Contrast agents for molecular photoacoustic imaging. *Nat. Methods* **2016**, *13*, 639–650.
- (2) Liu, H.; Hu, Y.; Sun, Y.; Wan, C.; Zhang, Z.; Dai, X.; Lin, Z.; He, Q.; Yang, Z.; Huang, P.; Xiong, Y.; Cao, J.; Chen, X.; Chen, Q.; Lovell, J. F.; Xu, Z.; Jin, H.; Yang, K. Co-delivery of Bee Venom Melittin and a Photosensitizer with an Organic—Inorganic Hybrid Nanocarrier for Photodynamic Therapy and Immunotherapy. *ACS Nano* 2019, 13, 12638–12652.
- (3) Guo, J.; Agola, J. O.; Serda, R.; Franco, S.; Lei, Q.; Wang, L.; Minster, J.; Croissant, J. G.; Butler, K. S.; Zhu, W.; Brinker, C. J. Biomimetic Rebuilding of Multifunctional Red Blood Cells: Modular Design Using Functional Components. *ACS Nano* **2020**, *14*, 7847–7859.
- (4) Cao, J.; Zaremba, O. T.; Lei, Q.; Ploetz, E.; Wuttke, S.; Zhu, W. Artificial Bioaugmentation of Biomacromolecules and Living Organisms for Biomedical Applications. *ACS Nano* **2021**, *15*, 3900–3926.
- (5) Guo, J.; Amini, S.; Lei, Q.; Ping, Y.; Agola, J. O.; Wang, L.; Zhou, L.; Cao, J.; Franco, S.; Noureddine, A.; Miserez, A.; Zhu, W.; Brinker, C. J. Robust and Long-Term Cellular Protein and Enzymatic Activity Preservation in Biomineralized Mammalian Cells. *ACS Nano* **2022**, *16*, 2164–2175.
- (6) Wang, Y.; Du, W.; Zhang, T.; Zhu, Y.; Ni, Y.; Wang, C.; Sierra Raya, F. M.; Zou, L.; Wang, L.; Liang, G. A Self-Evaluating Photothermal Therapeutic Nanoparticle. *ACS Nano* **2020**, *14*, 9585–9593.
- (7) Chen, J.; Ma, Y.; Du, W.; Dai, T.; Wang, Y.; Jiang, W.; Wan, Y.; Wang, Y.; Liang, G.; Wang, G. Furin-Instructed Intracellular Gold Nanoparticle Aggregation for Tumor Photothermal Therapy. *Adv. Funct. Mater.* **2020**, *30*, 2001566.
- (8) Zhou, J.; Creyer, M. N.; Chen, A.; Yim, W.; Lafleur, R. P. M.; He, T.; Lin, Z.; Xu, M.; Abbasi, P.; Wu, J.; Pascal, T. A.; Caruso, F.; Jokerst, J. V. Stereoselective Growth of Small Molecule Patches on Nanoparticles. *J. Am. Chem. Soc.* **2021**, *143*, 12138–12144.
- (9) Jin, Z.; Mantri, Y.; Retout, M.; Cheng, Y.; Zhou, J.; Jorns, A.; Fajtova, P.; Yim, W.; Moore, C.; Xu, M.; Creyer, M.; Borum, R.; Zhou, J.; Wu, Z.; He, T.; Penny, W.; O'Donoghue, A.; Jokerst, J. A Charge-Switchable Zwitterionic Peptide for Rapid Detection of

- SARS-CoV-2 Main Protease. Angew. Chem., Int. Ed. 2021, 61, No. e202112995.
- (10) Lee, J. E.; Lee, N.; Kim, T.; Kim, J.; Hyeon, T. Multifunctional Mesoporous Silica Nanocomposite Nanoparticles for Theranostic Applications. *Acc. Chem. Res.* **2011**, *44*, 893–902.
- (11) Wu, Z.; Zhou, J.; Nkanga, C. I.; Jin, Z.; He, T.; Borum, R. M.; Yim, W.; Zhou, J.; Cheng, Y.; Xu, M.; Steinmetz, N. F.; Jokerst, J. V. One-Step Supramolecular Multifunctional Coating on Plant Virus Nanoparticles for Bioimaging and Therapeutic Applications. *ACS Appl. Mater. Interfaces* **2022**, *14*, 13692–13702.
- (12) Du, L.; Nosratabad, N. A.; Jin, Z.; Zhang, C.; Wang, S.; Chen, B.; Mattoussi, H. Luminescent Quantum Dots Stabilized by N-Heterocyclic Carbene Polymer Ligands. *J. Am. Chem. Soc.* **2021**, *143*, 1873–1884.
- (13) Wang, S.; Du, L.; Jin, Z.; Xin, Y.; Mattoussi, H. Enhanced Stabilization and Easy Phase Transfer of CsPbBr₃ Perovskite Quantum Dots Promoted by High-Affinity Polyzwitterionic Ligands. *J. Am. Chem. Soc.* **2020**, *142*, 12669–12680.
- (14) Zhan, N.; Palui, G.; Merkl, J.-P.; Mattoussi, H. Bio-orthogonal Coupling as a Means of Quantifying the Ligand Density on Hydrophilic Quantum Dots. *J. Am. Chem. Soc.* **2016**, *138*, 3190–3201.
- (15) Ding, Z.; Sun, H.; Ge, S.; Cai, Y.; Yuan, Y.; Hai, Z.; Tao, T.; Hu, J.; Hu, B.; Wang, J.; Liang, G. Furin-Controlled Fe₃O₄ Nanoparticle Aggregation and 19F Signal "Turn-On" for Precise MR Imaging of Tumors. *Adv. Funct. Mater.* **2019**, *29*, 1903860.
- (16) Wang, Y.; Li, X.; Chen, P.; Dong, Y.; Liang, G.; Yu, Y. Enzyme-instructed self-aggregation of Fe_3O_4 nanoparticles for enhanced MRI T_2 imaging and photothermal therapy of tumors. *Nanoscale* **2020**, *12*, 1886–1893.
- (17) Jokerst, J. V.; Khademi, C.; Gambhir, S. S. Intracellular Aggregation of Multimodal Silica Nanoparticles for Ultrasound-Guided Stem Cell Implantation. *Sci. Transl. Med.* **2013**, *5*, 177ra35.
- (18) Cheng, P.; Pu, K. Molecular imaging and disease theranostics with renal-clearable optical agents. *Nat. Rev. Mater.* **2021**, *6*, 1095–1113.
- (19) Park, J. H.; Gu, L.; von Maltzahn, G.; Ruoslahti, E.; Bhatia, S. N.; Sailor, M. J. Biodegradable luminescent porous silicon nanoparticles for in vivo applications. *Nat. Mater.* **2009**, *8*, 331–336.
- (20) Liew, S. S.; Zeng, Z.; Cheng, P.; He, S.; Zhang, C.; Pu, K. Renal-Clearable Molecular Probe for Near-Infrared Fluorescence Imaging and Urinalysis of SARS-CoV-2. *J. Am. Chem. Soc.* **2021**, *143*, 18827–18831.
- (21) Huang, J.; Jiang, Y.; Li, J.; He, S.; Huang, J.; Pu, K. A Renal-Clearable Macromolecular Reporter for Near-Infrared Fluorescence Imaging of Bladder Cancer. *Angew. Chem., Int. Ed.* **2020**, *59*, 4415–4420
- (22) Nafiujjaman, M.; Chung, S.-J.; Kalashnikova, I.; Hill, M. L.; Homa, S.; George, J.; Contag, C. H.; Kim, T. Biodegradable Hollow Manganese Silicate Nanocomposites to Alleviate Tumor Hypoxia toward Enhanced Photodynamic Therapy. *ACS Appl. Bio Mater.* **2020**, *3*, 7989–7999.
- (23) Lyu, Y.; Zeng, J.; Jiang, Y.; Zhen, X.; Wang, T.; Qiu, S.; Lou, X.; Gao, M.; Pu, K. Enhancing Both Biodegradability and Efficacy of Semiconducting Polymer Nanoparticles for Photoacoustic Imaging and Photothermal Therapy. *ACS Nano* **2018**, *12*, 1801–1810.
- (24) Liang, Y.; Sun, H.; Cao, W.; Thompson, M. P.; Gianneschi, N. C. Degradable Polyphosphoramidate via Ring-Opening Metathesis Polymerization. *ACS Macro Lett.* **2020**, *9*, 1417–1422.
- (25) Lovell, J. F.; Jin, C. S.; Huynh, E.; MacDonald, T. D.; Cao, W.; Zheng, G. Enzymatic Regioselection for the Synthesis and Biodegradation of Porphysome Nanovesicles. *Angew. Chem., Int. Ed.* **2012**, *51*, 2429–2433.
- (26) Sun, H.; Liang, Y.; Thompson, M. P.; Gianneschi, N. C. Degradable polymers via olefin metathesis polymerization. *Prog. Polym. Sci.* **2021**, 120, 101427.
- (27) Sun, H.; Yan, L.; Carter, K. A.; Zhang, J.; Caserto, J. S.; Lovell, J. F.; Wu, Y.; Cheng, C. Zwitterionic Cross-Linked Biodegradable Nanocapsules for Cancer Imaging. *Langmuir* **2019**, *35*, 1440–1449.

- (28) Sun, H.; Yan, L.; Chang, M. Y. Z.; Carter, K. A.; Zhang, R.; Slyker, L.; Lovell, J. F.; Wu, Y.; Cheng, C. A multifunctional biodegradable brush polymer-drug conjugate for paclitaxel/gemcitabine co-delivery and tumor imaging. *Nanoscale Adv.* **2019**, *1*, 2761–2771.
- (29) Altinoğlu, E. I.; Russin, T. J.; Kaiser, J. M.; Barth, B. M.; Eklund, P. C.; Kester, M.; Adair, J. H. Near-infrared emitting fluorophore-doped calcium phosphate nanoparticles for in vivo imaging of human breast cancer. *ACS Nano* **2008**, *2*, 2075–2084.
- (30) Tang, J.; Li, L.; Howard, C. B.; Mahler, S. M.; Huang, L.; Xu, Z. P. Preparation of optimized lipid-coated calcium phosphate nanoparticles for enhanced in vitro gene delivery to breast cancer cells. *J. Mater. Chem. B* **2015**, *3*, 6805–6812.
- (31) Liu, Z.; Xiao, Y.; Chen, W.; Wang, Y.; Wang, B.; Wang, G.; Xu, X.; Tang, R. Calcium phosphate nanoparticles primarily induce cell necrosis through lysosomal rupture: the origination of material cytotoxicity. *J. Mater. Chem. B* **2014**, *2*, 3480–3489.
- (32) Abou Neel, E. A.; Pickup, D. M.; Valappil, S. P.; Newport, R. J.; Knowles, J. C. Bioactive functional materials: a perspective on phosphate-based glasses. *J. Mater. Chem.* **2009**, *19*, 690–701.
- (33) Knowles, J. C. Phosphate based glasses for biomedical applications. J. Mater. Chem. 2003, 13, 2395.
- (34) Foroutan, F.; Jokerst, J. V.; Gambhir, S. S.; Vermesh, O.; Kim, H.-W.; Knowles, J. C. Sol–Gel Synthesis and Electrospraying of Biodegradable (P₂O₅)₅₅–(CaO)₃₀–(Na₂O)₁₅ Glass Nanospheres as a Transient Contrast Agent for Ultrasound Stem Cell Imaging. *ACS Nano* **2015**, *9*, 1868–1877.
- (35) Santos, E. M.; Radin, S.; Ducheyne, P. Sol-gel derived carrier for the controlled release of proteins. *Biomaterials* **1999**, *20*, 1695–1700
- (36) Govindan, R.; Girija, E. K. Drug loaded phosphate glass/hydroxyapatite nanocomposite for orthopedic applications. *J. Mater. Chem. B* **2014**, *2*, 5468–5477.
- (37) Casciaro, S.; Conversano, F.; Ragusa, A.; Malvindi, M.; Franchini, R.; Greco, A.; Pellegrino, T.; Gigli, G. Optimal Enhancement Configuration of Silica Nanoparticles for Ultrasound Imaging and Automatic Detection at Conventional Diagnostic Frequencies. *Invest. Radiol.* **2010**, *45*, 715–724.
- (38) Errico, C.; Pierre, J.; Pezet, S.; Desailly, Y.; Lenkei, Z.; Couture, O.; Tanter, M. Ultrafast ultrasound localization microscopy for deep super-resolution vascular imaging. *Nature* **2015**, *527*, 499–502.
- (39) Demené, C.; Robin, J.; Dizeux, A.; Heiles, B.; Pernot, M.; Tanter, M.; Perren, F. Transcranial ultrafast ultrasound localization microscopy of brain vasculature in patients. *Nat. Biomed. Eng.* **2021**, *5*, 219–228.
- (40) He, T.; Bradley, D. G.; Zhou, J.; Jorns, A.; Mantri, Y.; Hanna, J. V.; Jokerst, J. V. Hydro-Expandable Calcium Phosphate Micro/Nano-Particles with Controllable Size and Morphology for Mechanical Ablation. *ACS Appl. Nano Mater.* **2021**, *4*, 3877–3886.
- (41) He, T.; Jokerst, J. V. Structured micro/nano materials synthesized via electrospray: a review. *Biomater. Sci.* **2020**, *8*, 5555–5573.
- (42) Sumper, M.; Brunner, E. Learning from Diatoms: Nature's Tools for the Production of Nanostructured Silica. *Adv. Funct. Mater.* **2006**, *16*, 17–26.
- (43) Sumper, M.; Kröger, N. Silica formation in diatoms: the function of long-chain polyamines and silaffins. *J. Mater. Chem.* **2004**, 14, 2059–2065.
- (44) Antonietti, L.; Aymonier, C.; Schlotterbeck, U.; Garamus, V. M.; Maksimova, T.; Richtering, W.; Mecking, S. Core-Shell-Structured Highly Branched Poly(ethylenimine amide)s: Synthesis and Structure. *Macromolecules* **2005**, *38*, 5914–5920.
- (45) Lei, Q.; Guo, J.; Kong, F.; Cao, J.; Wang, L.; Zhu, W.; Brinker, C. J. Bioinspired Cell Silicification: From Extracellular to Intracellular. *J. Am. Chem. Soc.* **2021**, *143*, 6305–6322.
- (46) Pickup, D. M.; Guerry, P.; Moss, R. M.; Knowles, J. C.; Smith, M. E.; Newport, R. J. New sol-gel synthesis of a (CaO)_{0.3}(Na₂O)_{0.2}(P₂O₅)_{0.5} bioresorbable glass and its structural characterisation. *J. Mater. Chem.* **2007**, *17*, 4777.

- (47) Benjaminsen, R. V.; Mattebjerg, M. A.; Henriksen, J. R.; Moghimi, S. M.; Andresen, T. L. The Possible "Proton Sponge" Effect of Polyethylenimine (PEI) Does Not Include Change in Lysosomal pH. *Mol. Ther.* **2013**, *21*, 149–157.
- (48) Yeh, P.-H.; Sun, J.-S.; Wu, H.-C.; Hwang, L.-H.; Wang, T.-W. Stimuli-responsive HA-PEI nanoparticles encapsulating endostatin plasmid for stem cell gene therapy. *RSC Adv.* **2013**, *3*, 12922–12932.
- (49) Jin, Z.; Du, L.; Zhang, C.; Sugiyama, Y.; Wang, W.; Palui, G.; Wang, S.; Mattoussi, H. Modification of poly (maleic anhydride)-based polymers with H₂N–R nucleophiles: Addition or substitution reaction? *Bioconjugate Chem.* **2019**, *30*, 871–880.
- (50) Catti, M.; Ferraris, G.; Filhol, A. Hydrogen bonding in the crystalline state. CaHPO₄ (monetite), P1 or P1? A novel neutron diffraction study. *Acta Crystallogr., Sect. B: Struct. Crystallogr. Cryst. Chem.* 1977, 33, 1223–1229.
- (51) Curry, N. A.; Jones, D. W. Crystal structure of brushite, calcium hydrogen orthophosphate dihydrate: a neutron-diffraction investigation. *J. Chem. Soc. A* **1971**, 3725–3729.
- (52) Dickens, B.; Prince, E.; Schroeder, L. W.; Brown, W. E. Ca(H₂PO₄)₂, a crystal structure containing unusual hydrogen bonding. *Acta Crystallogr., Sect. B: Struct. Crystallogr. Cryst. Chem.* 1973, 29, 2057–2070.
- (53) Liu, S.; Liang, Y.; Ma, X.; Li, H.; Zhang, W.; Tu, D.; Chen, Y. Tunable Photoluminescence and Energy Transfer Efficiency in β -Ca₃(PO₄)₂-Ca₉La(PO₄)₇:Eu²⁺, Mn²⁺ Solid Solution Phosphors Introduced by Emptying Site and Structural Confinement Effect for Solid-State Lighting Application. *Inorg. Chem.* **2020**, *59*, 3596–3605.
- (54) Mathew, M.; Brown, W. E.; Schroeder, L. W.; Dickens, B. Crystal structure of octacalcium bis(hydrogenphosphate) tetrakis-(phosphate)pentahydrate, Ca₈(HPO₄)₂(PO₄)4·SH₂O. *J. Crystallogr. Spectrosc. Res.* **1988**, *18*, 235–250.
- (55) Mathew, M.; Schroeder, L. W.; Dickens, B.; Brown, W. E. The crystal structure of α -Ca₃(PO₄)₂. Acta Crystallogr., Sect. B: Struct. Crystallogr. Cryst. Chem. **1977**, 33, 1325–1333.
- (56) Schroeder, L. W.; Prince, E.; Dickens, B. Hydrogen bonding in Ca(H₂PO₄)₂.H₂O as determined by neutron diffraction. *Acta Crystallogr., Sect. B: Struct. Crystallogr. Cryst. Chem.* **1975**, 31, 9–12.
- (57) Tanaka, Y.; Iwasaki, T.; Katayama, K.; Hojo, J.; Yamashita, K. Effect of Ionic Polarization on Crystal Structure of Hydroxyapatite Ceramic with Hydroxide Nonstoichiometry. *J. Jpn. Soc. Powder Powder Metall.* **2010**, *57*, 520–528.
- (58) Brow, R. K. Review: the structure of simple phosphate glasses. *J. Non-Cryst. Solids* **2000**, 263–264, 1–28.
- (59) Sirsi, S.; Feshitan, J.; Kwan, J.; Homma, S.; Borden, M. Effect of microbubble size on fundamental mode high frequency ultrasound imaging in mice. *Ultrasound Med. Biol.* **2010**, *36*, 935–948.
- (60) Casciaro, S.; Conversano, F.; Ragusa, A.; Ada Malvindi, M.; Franchini, R.; Greco, A.; Pellegrino, T.; Gigli, G. Optimal Enhancement Configuration of Silica Nanoparticles for Ultrasound Imaging and Automatic Detection at Conventional Diagnostic Frequencies. *Invest. Radiol.* **2010**, *45*, 715–724.
- (61) Pastor-Pérez, L.; Chen, Y.; Shen, Z.; Lahoz, A.; Stiriba, S. E. Unprecedented Blue Intrinsic Photoluminescence from Hyperbranched and Linear Polyethylenimines: Polymer Architectures and pH-Effects. *Macromol. Rapid Commun.* **2007**, 28, 1404–1409.
- (62) Kempen, P. J.; Greasley, S.; Parker, K. A.; Campbell, J. L.; Chang, H. Y.; Jones, J. R.; Sinclair, R.; Gambhir, S. S.; Jokerst, J. V. Theranostic mesoporous silica nanoparticles biodegrade after prosurvival drug delivery and ultrasound/magnetic resonance imaging of stem cells. *Theranostics* **2015**, *5*, 631–642.
- (63) Hunter, A. C. Molecular hurdles in polyfectin design and mechanistic background to polycation induced cytotoxicity. *Adv. Drug Deliv. Rev.* **2006**, *58*, 1523–1531.
- (64) Gottlieb, H. E.; Kotlyar, V.; Nudelman, A. NMR chemical shifts of common laboratory solvents as trace impurities. *J. Org. Chem.* **1997**, 62, 7512–7515.
- (65) Huang, X.; Zhu, Y.; Zhang, X.; Bao, Z.; Lei, D. Y.; Yu, W.; Dai, J.; Wang, Y. Clam-inspired nanoparticle immobilization method using

adhesive tape as microchip substrate. Sens. Actuators, B 2016, 222, 106–111.

TRecommended by ACS

Piezoelectric Nanoparticles for Ultrasound-Based Wireless Therapies

Jayanta Dolai, Nikhil R. Jana, et al.

OCTOBER 10, 2022

ACS APPLIED NANO MATERIALS

READ 🗹

Assembling Biocompatible Polymers on Gold Nanoparticles: Toward a Rational Design of Particle Shape by Molecular Dynamics

Roberta Cappabianca, Pietro Asinari, et al.

NOVEMBER 10, 2022

ACS OMEGA

READ 🗹

Surface-Active Plasma-Polymerized Nanoparticles for Multifunctional Diagnostic, Targeting, and Therapeutic Probes

Laura L. Haidar, Behnam Akhavan, et al.

AUGUST 30, 2022

ACS APPLIED NANO MATERIALS

READ 🗹

Self-Fueled Janus Nanomotors as Active Drug Carriers for Propulsion Behavior-Reinforced Permeability and Accumulation at the Tumor Site

Wenjun Chen, Xing Ma, et al.

AUGUST 01, 2022

CHEMISTRY OF MATERIALS

READ 🗹

Get More Suggestions >